



<b>Publication Year</b>	2017
<b>Acceptance in OA</b>	2020-07-22T05:32:06Z
<b>Title</b>	ALMA survey of massive cluster progenitors from ATLASGAL. Limited fragmentation at the early evolutionary stage of massive clumps
<b>Authors</b>	Csengeri, T., Bontemps, S., Wyrowski, F., Motte, F., Menten, K. M., Beuther, H., Bronfman, L., Commerçon, B., Chapillon, E., Duarte-Cabral, A., Fuller, G. A., Henning, Th., Leurini, Silvia, Longmore, S., Palau, A., Peretto, N., Schuller, F., Tan, J. C., Testi, L., TRAFICANTE, ALESSIO, Urquhart, J. S.
<b>Publisher's version (DOI)</b>	10.1051/0004-6361/201629754
<b>Handle</b>	<a href="http://hdl.handle.net/20.500.12386/26555">http://hdl.handle.net/20.500.12386/26555</a>
<b>Journal</b>	ASTRONOMY & ASTROPHYSICS
<b>Volume</b>	600

LETTER TO THE EDITOR

# ALMA survey of massive cluster progenitors from ATLASGAL

## Limited fragmentation at the early evolutionary stage of massive clumps

T. Csengeri<sup>1</sup>, S. Bontemps<sup>2</sup>, F. Wyrowski<sup>1</sup>, F. Motte<sup>3,4</sup>, K. M. Menten<sup>1</sup>, H. Beuther<sup>5</sup>, L. Bronfman<sup>6</sup>, B. Commerçon<sup>7</sup>, E. Chapillon<sup>2,8</sup>, A. Duarte-Cabral<sup>9,13</sup>, G. A. Fuller<sup>10</sup>, Th. Henning<sup>5</sup>, S. Leurini<sup>1</sup>, S. Longmore<sup>11</sup>, A. Palau<sup>12</sup>, N. Peretto<sup>13</sup>, F. Schuller<sup>1</sup>, J. C. Tan<sup>14</sup>, L. Testi<sup>15,16</sup>, A. Traficante<sup>17</sup>, and J. S. Urquhart<sup>18</sup>

(Affiliations can be found after the references)

Received , 2016; accepted , 2016

### ABSTRACT

The early evolution of massive cluster progenitors is poorly understood. We investigate the fragmentation properties from 0.3 pc to 0.06 pc scales of a homogenous sample of infrared-quiet massive clumps within 4.5 kpc selected from the ATLASGAL survey. Using the ALMA 7m array we detect compact dust continuum emission towards all targets, and find that fragmentation, at these scales, is limited. The mass distribution of the fragments uncovers a large fraction of cores above  $40 M_{\odot}$ , corresponding to massive dense cores (MDCs) with masses up to  $\sim 400 M_{\odot}$ . 77% of the clumps contain at most 3 MDCs per clump, and we also reveal single clumps/MDCs. The most massive cores are formed within the more massive clumps, and a high concentration of mass on small scales reveals a high core formation efficiency. The mass of MDCs highly exceeds the local thermal Jeans-mass, and observational evidence is lacking for a sufficiently high level of turbulence or strong enough magnetic fields to keep the most massive MDCs in equilibrium. If already collapsing, the observed fragmentation properties with a high core formation efficiency are consistent with the collapse setting in at parsec scales.

**Key words.** stars: massive – stars: formation – submillimeter: ISM

### 1. Introduction

The properties and the evolution of massive clumps hosting the precursors of the highest mass stars currently forming in our Galaxy are poorly known. Massive clumps at an early evolutionary phase, thus, prior to the emergence of luminous massive young stellar objects and UC-H II regions, are excellent candidates to host high-mass protostars in their earliest stages (e.g. Zhang et al. 2009; Bontemps et al. 2010; Csengeri et al. 2011a,b; Palau et al. 2013; Sánchez-Monge et al. 2013). Large samples have only recently been identified based on large area surveys (e.g. Butler & Tan 2012; Tackenberg et al. 2012; Traficante et al. 2015; Svoboda et al. 2016; Csengeri et al. 2017), which show that the early evolutionary stages are short lived (e.g. Motte et al. 2007; Csengeri et al. 2014), as star formation proceeds rapidly. Using the Atacama Large Millimeter/submillimeter Array (ALMA), here we present the first results of a statistical study of early stage fragmentation to shed light on the physical processes at the origin of high-mass collapsing entities, and to search for the youngest precursors of O-type stars.

### 2. The sample of infrared quiet massive clumps

Based on a flux limited sample of the 870  $\mu\text{m}$  APEX Telescope Large Survey of the Galaxy (ATLASGAL, Schuller et al. 2009; Csengeri et al. 2014), Csengeri et al. (2017) identified the complete sample of massive infrared quiet clumps with the highest peak surface density ( $\Sigma_{\text{cl}} \geq 0.5 \text{ g cm}^{-2}$ )<sup>1</sup> and low bolometric luminosity,  $L_{\text{bol}} < 10^4 L_{\odot}$ , corresponding to the ZAMS luminosity

of a late O type star. Their large mass reservoir and low luminosity suggest that infrared quiet massive clumps correspond to the early evolutionary phase, some already exhibiting signs of ongoing (high-mass) star formation such as EGOs and Class II methanol masers. Here we present the sample of 35 infrared quiet massive clumps located within  $d \leq 4.5 \text{ kpc}$ , which could be conveniently grouped on the sky as targets for ALMA. They cover 70% of all the most massive and nearby infrared quiet clumps from Csengeri et al. (2017), and are thus a representative selection of a homogenous sample of early phase massive clumps in the inner Galaxy.

### 3. Observations and data reduction

We present observations carried out in Cycle 2 with the ALMA 7m array using 9 to 11 of the 7m antennas with baselines ranging between 8.2 m (9.5k $\lambda$ ) to 48.9 m (53.4k $\lambda$ ). We used a low-resolution wide-band setup in Band 7, yielding  $4 \times 1.75 \text{ GHz}$  effective bandwidth with a spectral resolution of 976.562 kHz. The four basebands were centred on 347.331, 345.796, 337.061, 335.900 GHz, respectively. The primary beam at this frequency is 28.9''. Each source was observed for  $\sim 5.4 \text{ min}$  in total. The system temperature,  $T_{\text{sys}}$  varies between 100–150 K. The targets have been split according to Galactic longitude in five observing groups (Table 1).

The data was calibrated using standard procedures in CASA 4.2.1. To obtain line-free continuum images, we first identified the channels with spectral lines towards each source, and excluding these averaged the remaining channels. We used a robust weight of 0.5 for imaging, and the CLEAN algorithm for the deconvolution, and corrected for the primary beam attenuation. The synthesized beam varies between 3.5'' to 4.6'' taking

<sup>1</sup> In the ATLASGAL beam of 19''.2.

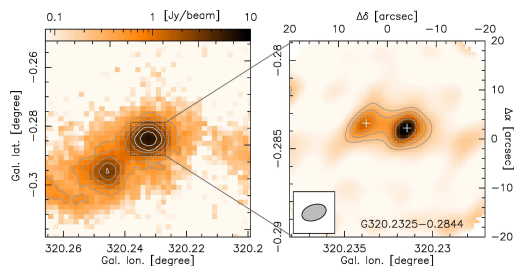


Fig. 1: *Left*: Clump-scale view by ATLASGAL of an example source. *Right*: Line-free continuum emission at 345 GHz by the ALMA 7m array. Contours start at  $7\sigma_{\text{rms}}$  noise and increase in a logarithmic scale. White crosses mark the extracted sources (see Table 2). The synthesized beam is shown in the lower left corner.

the geometric mean of the major and minor axes. The noise has been measured in an emission free area close to the center of the maps including the side-lobes. The achieved median *rms* noise level is 54 mJy/beam and varies among the targets due to a combination of restricted bandwidth available for continuum, dynamic range or mediocre observing conditions. In particular for groups 4 and 5, the observations have been carried out at low elevation resulting in an elongated beam and poor *uv*-sampling. The observing parameters per group are summarized in Table 1, and for each source in Table 2.

#### 4. Results and analysis

Compact continuum emission is detected towards all clumps (see Fig. 1 for an example, and Fig. A.1 for all targets). We find sources that stay single ( $\sim 14\%$ ) at our resolution and sensitivity. Fragmentation is, in fact, limited towards the majority of the sample; 45% of the clumps hosts up to two, while 77% host up to three compact sources. Only a few clumps host more fragments.

We identify and measure the parameters of the compact sources using the Gaussclumps task in GILDAS<sup>2</sup>, which performs a 2D Gaussian fitting. A total number of 124 fragments down to a  $\sim 7\sigma_{\text{rms}}$  noise level are systematically identified within the primary beam, where the noise is measured towards each field. This gives on average,  $\bar{N}_{\text{fr}}=3$  sources per clump corresponding to a population of cores at the typically achieved physical resolution of  $\sim 0.06$  pc.

We can directly compare the integrated flux in compact sources seen by the ALMA 7m array with the ATLASGAL flux densities measured over the primary beam of the array as both datasets have similar centre frequencies<sup>3</sup>. We recover between 16–47% of the flux, the rest of the emission is filtered above the typically  $19''$  largest angular scale sensitivity of the ALMA 7m array observations.

To estimate the mass, we assume optically thin dust emission and use the same formula as in Csengeri et al. (2017);  $M = S_{870\mu\text{m}} d^2 \kappa_{870\mu\text{m}}^{-1} B_{870\mu\text{m}}(T_d)^{-1}$ , where  $S_{870\mu\text{m}}$  is the integrated flux density,  $d$  is the distance,  $\kappa_{870\mu\text{m}} = 0.0185 \text{ g cm}^{-2}$  from Ossenkopf & Henning (1994) accounting for a gas-to-dust ratio of 100, and  $B_{\nu}(T_d)$  is the Planck function. While on the  $\sim 0.3$  pc scales of clumps Csengeri et al. (2017) adopt  $T_d=18$  K,

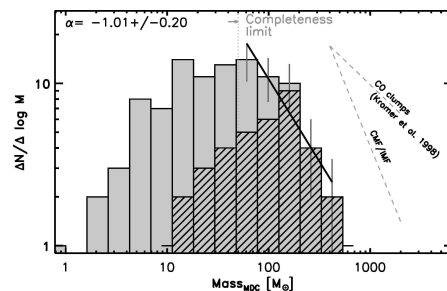


Fig. 2: Mass distribution of MDCs within  $d \leq 4.5$  kpc. The Poisson error of each bin is shown as a grey line above the  $10\sigma_{\text{rms}}$  completeness limit of  $50 M_{\odot}$ , the power-law fit is shown in a solid black line. Hatched area shows the distribution of the brightest cores ( $M_{\text{MDC}}^{\text{max}}$ ) per clump. Dashed lines show the slope of the CMF/IMF (André et al. 2014), and CO clumps (Kramer et al. 1998).

on the smaller scales of cores heating due to the embedded proto-star may result in elevated dust temperatures that are poorly constrained. Following the model of Goldreich & Kwan (1974), we estimate  $T_d=15$ – $38$  K for the luminosity range of  $10^2 - 10^4 L_{\odot}$  at a typical radius of half the deconvolved *FWHM* size of  $0.025$  pc. We adopt thus  $T_d=25$  K which results up to a factor of two uncertainty in the mass estimate.

The extracted cores have a mean mass of  $\sim 63 M_{\odot}$  corresponding to massive dense cores (MDCs as in Motte et al. 2007), and about 40% of the sample hosts cores more massive than  $150 M_{\odot}$ . They are, in terms of physical properties, similar to SDC335-MM1 (Peretto et al. 2013), which is here the most massive core with  $\sim 400 M_{\odot}$  within a deconvolved *FWHM* size of  $0.054 \text{ pc}^4$ . In these clumps the second brightest sources are also typically massive, on average  $78 M_{\odot}$  suggesting a preference to form more massive cores. Except for one clump, no core is detected below  $35 M_{\odot}$  which is well above the typical detection threshold considering the mean  $7\sigma_{\text{rms}}$  mass sensitivity of  $11.2 M_{\odot}$  at the mean distance of  $2.6$  kpc, and may indicate a lack of intermediate mass (between  $10$ – $40 M_{\odot}$ ) cores. Similar findings have been reported towards a handful of other young massive sources by Bontemps et al. (2010) and Zhang et al. (2015). Clumps with single sources host strictly massive cores with  $M_{\text{MDC}} > 40 M_{\odot}$ , and about half of them reaches the highest mass range of  $M_{\text{MDC}} > 150 M_{\odot}$ .

We show the mass distribution of cores as  $\Delta N / \Delta \log M \sim M^{\alpha}$  in Fig. 2, and indicate the  $10\sigma_{\text{rms}}$  completeness limit of  $50 M_{\odot}$ , set by the highest noise in the poorest sensitivity data. The distribution tends to be flat up to the completeness limit, and then shows a decrease at the highest masses. The distribution of  $M_{\text{MDC}}^{\text{max}}$  (hatched histogram) shows that the majority of the clumps host at least one massive core, while a few host only at most intermediate mass fragments. The least square power-law fit to the highest mass bins above the completeness limit gives  $\alpha = -1.01 \pm 0.20$ , which is steeper than the distribution of CO clumps ( $\alpha = -0.6$  to  $-0.8$ , Kramer et al. 1998), and tends to be shallower than the low-mass prestellar CMF and the stellar initial mass function (IMF) ( $\alpha = -1.35$ – $-1.5$ , André et al. 2010), although at the high-mass end the scatter of the measured slopes is more significant (Bastian et al. 2010). Using Monte Carlo methods we test the uncertainty of  $\alpha$  due to the unknown dust temperature, and simulated a range of  $T_d$  between  $10$ – $50$  K using a

<sup>2</sup> Continuum and Line Analysis Single-Dish Software <http://www.iram.fr/IRAMFR/GILDAS>

<sup>3</sup> The centre frequency for the ALMA dataset is at  $341.4$  GHz, while for the LABOCA filter, it is around  $345$  GHz. A spectral index of  $-3.5$  gives 10% change in the flux up to a difference of  $10$  GHz in the centre frequencies. This is below our absolute flux uncertainty.

<sup>4</sup> Our mass estimates for SDC335-MM1 can be reconciled with Peretto et al. (2013) using a dust emissivity index of  $\beta \sim 1.2$  between  $93$  GHz and  $345$  GHz. A similarly low value of  $\beta$  is also suggested by Avison et al. (2015).

Table 1: Summary of observations.

Observing group	Date	Bandpass calibrator	Phase calibrator	Flux calibrator	Synthesized beam <sup>a</sup>	$\sigma_{\text{rms}}$ <sup>b</sup>
1	320 < $\ell$ < 330°	8, 16 July 2014	J1427-4206	J16170-5848	Titan, Ceres	$5.0 \times 2.9$ -78.6 3.8 19.3 – 83.5
2	330 < $\ell$ < 340°	18, 21 July 2014	J1427-4206	J1617-5848	Titan, Ceres	$4.6 \times 2.8$ 14.9 3.6 20.7 – 119.2
3	340 < $\ell$ < 350°	19, 21 July 2014	J1517-2422	J1636-4102	Titan, Ceres	$4.7 \times 2.6$ -83.4 3.5 22.9 – 105.3
4	350 < $\ell$ < 360°	14, 15 June 2014	J1733-1304	J1717-3342	Neptune	$9.2 \times 2.4$ -76.2 4.6 28.7 – 175.8
5	30 < $\ell$ < 40°	8 June 2014	J1751+0939	J1851+0035	Neptune	$5.8 \times 2.4$ -68.2 3.7 16.4 – 45.8

**Notes.** <sup>(a)</sup> Averaged properties. <sup>(b)</sup> The minimum and maximum  $\sigma_{\text{rms}}$  noise is averaged over the line-free channels in the total 7.5 GHz bandwidth.

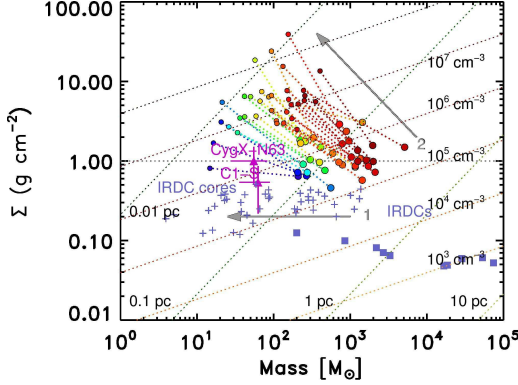


Fig. 3: Surface-density versus mass diagram, coloured dotted lines in different shades show constant radius (green) and  $n_{\text{H}}$  number density (red) (c.f. Tan et al. 2014). Colored large circles show clumps (ATLASGAL), while smaller circles the cores (ALMA 7m array), colors scaling from blue to red with increasing  $M_{\text{MDC}}^{\text{max}}$ . We mark two massive cores with  $M_{\text{MDC}} = 60 M_{\odot}$  (C1-S, Tan et al. 2013) and  $55 M_{\odot}$  (CygX-N63, Bontemps et al. 2010). For comparison IRDC clumps (Kainulainen & Tan 2013) and cores are shown (Butler & Tan 2012). Gray arrows show two models: 1) a uniform clump density, and 2) a single central object with an  $r^{-2}$  density profile.

normal distribution with a mean of 25 K, and a power-law distribution. We fitted to the slope the same way, as above, and repeated the tests until the standard deviation of the measured slope reached convergence. In good agreement with the observational results, the normal temperature distribution gives  $\alpha_{\text{MC}} = -1.01 \pm 0.11$ , and thus constrains the error of the fit suggesting an intrinsically shallower slope than the IMF. A power-law temperature distribution in the same mass range with an exponent of  $-0.5$ , could reproduce, however, the slope of the IMF, assuming that the brightest sources are intrinsically warmer. Alternatively, a larger level of fragmentation of the brightest cores on smaller scales could also reconcile our result with the IMF.

## 5. Discussion

### 5.1. Limited fragmentation from clump to core scale

The thermal Jeans mass in massive clumps is low ( $M_{\text{J}} \sim 1 M_{\odot}$  at  $\bar{n}_{\text{cl}} = 4.6 \times 10^5 \text{ cm}^{-3}$ ,  $T = 18 \text{ K}$ ), which is expected to lead to a high degree of fragmentation. In contrast, the observed infrared quiet massive clumps exhibit here limited fragmentation with  $\bar{N}_{\text{fr}} = 3$ , from clump to core scales. We even find single clumps/MDCs at our resolution. This is intriguing also because these most massive clumps of the Galaxy are expected to form rich clusters. The selected highest peak surface density clumps could therefore correspond to a phase of compactness where the large level of fragmentation to form a cluster has not yet developed.

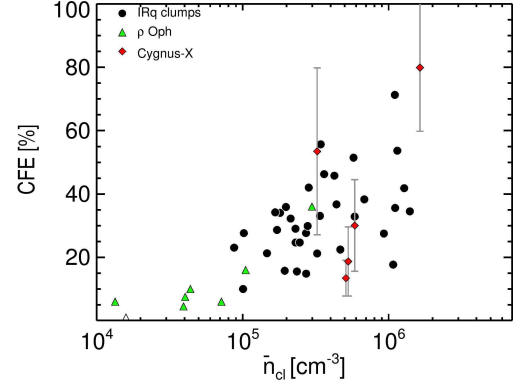


Fig. 4: CFE versus average clump density ( $\bar{n}_{\text{cl}}$ ). Green triangles show cores of  $\rho$  Oph (Motte et al. 1998) and red diamonds of Cygnus-X (Bontemps et al. 2010).

We find that the mass surface density ( $\Sigma$ ) increases towards small scales (Fig. 3, c.f. Tan et al. 2014) corresponding to a high concentration of mass. 80% of the clumps host MDCs above  $40 M_{\odot}$ , and the most massive fragments scale with the mass of their clump. Two models are shown with arrows in Fig. 3: 1) clumps with a uniform mass distribution forming low mass stars correspond to a roughly constant mass surface density; 2) clumps with all the mass concentrated in a single object corresponding to  $n(r) \sim r^{-2}$  density profile. The majority of the sources fit better the steeper than uniform density profile.

The early fragmentation of massive clumps thus does not seem to follow thermal processes, and shows fragment masses largely exceeding the local Jeans-mass (see also Zhang et al. 2009; Bontemps et al. 2010; Wang et al. 2014; Beuther et al. 2015; Butler & Tan 2012). The significant concentration of mass on small scales also manifests in a high core formation efficiency (CFE), which is the ratio of the total mass in fragments and the total clump mass from Csengeri et al. (2017) adopting the same physical parameters (Fig. 4). The CFE suggests an increasing concentration of mass in cores with the average clump volume density ( $\bar{n}_{\text{cl}}$ ), a trend which has been seen, although inferred from smaller scales, towards high-mass infrared quiet MDCs in Cygnus-X (Bontemps et al. 2010), and low-mass cores in  $\rho$  Oph (Motte et al. 1998), and a sample of infrared bright MDCs (Palau et al. 2013). Although the CFE shows variations at high densities with  $\bar{n}_{\text{cl}} > 10^5 \text{ cm}^{-3}$ , exceptionally high CFE of over 50%, can only be reached towards the highest average clump densities.

### 5.2. Which physical processes influence fragmentation?

What can explain that the thermal Jeans mass does not represent well the observed fragmentation properties in the early stages?



A combination of turbulence, magnetic field, and radiative feedback could increase the necessary mass scale for fragmentation. Using the Turbulent Core model (McKee & Tan 2003) for cores with  $M_{\text{MDC}} > 150 M_{\odot}$  at the average radius of 0.025 pc, we estimate from their Eq. 18 a turbulent line-width of  $\Delta v_{\text{obs}} \gtrsim 6 \text{ km s}^{-1}$  at the surface of cores, which is a factor of two higher than the average  $\Delta v_{\text{obs}}$  at the clump scale (Wienen et al. 2015). The magnetic critical mass at the average clump density corresponds to  $M_{\text{mag}} < 400 M_{\odot}$  at the typically observed magnetic field values of 1 mG towards massive clumps (e.g. Falgarone et al. 2008; Girart et al. 2009; Cortes et al. 2016; Pillai et al. 2016) following Eq. 2.17 of Bertoldi & McKee (1992). This suggests that moderately strong magnetic fields could explain the large core masses, however, at the high core densities of  $\bar{n}_{\text{core}} = 4 \times 10^7 \text{ cm}^{-3}$  considerably stronger fields, at the order of  $B > 10 \text{ mG}$ , would be required to keep the most massive cores subcritical. Although radiative feedback could also limit fragmentation (e.g. Krumholz et al. 2007; Longmore et al. 2011), infrared quiet massive clumps are at the onset of star formation activity and we lack evidence for a potential deeply embedded population of low-mass protostars needed to heat up the collapsing gas.

### 5.3. Can global collapse explain the mass of MDCs?

The rather monolithic fashion of collapse suggests that fragmentation is at least partly determined already at the clump scale, which would be in agreement with observational signatures of global collapse of massive filaments (e.g. Schneider et al. 2010; Peretto et al. 2013). If entire cloud fragments undergo collapse, and equilibrium may not be reached on small scales leading to the observed limited fragmentation and a high core formation efficiency at early stages. Mass replenishment beyond the clump scale could fuel the formation of the lower mass population of stars leading to an increase in the number of fragments with time, and allowing a Jeans-like fragmentation to develop at more evolved stages (e.g. Palau et al. 2015).

At the scale of cloud fragments, if collapse sets in at a lower density range of  $\bar{n}_{\text{cloud}} = 10^2 \text{ cm}^{-3}$ , the initial thermal Jeans mass could reach  $M_J \sim 50 M_{\odot}$  assuming  $T = 18 \text{ K}$ , at a characteristic  $\lambda_{\text{Jeans}}$  of about 2.3 pc. This is consistent with the extent of globally collapsing clouds, the involved mass range is, however, not sufficient to explain the mass reservoir of the most massive cores. Considering the turbulent nature of molecular clouds in the form of large-scale flows, their shocks could compress larger extents of gas at higher densities depending on the turbulent mach number (c.f. Chabrier & Hennebelle 2011), and lead to an increase in the initial mass reservoir. Fragmentation inhibition and the observed high CFE are thus consistent with a collapse setting in at parsec scales. The origin of their initial mass reservoir, however, still poses a challenge to current star formation models.

### 5.4. Towards the highest mass stars

The mass distribution of MDCs could be reconciled with the IMF either if multiplicity prevailed on smaller than 0.06 pc scales, or if the temperature distribution scales with the brightest fragments. Similar results have been found towards MDCs in Cygnus-X by Bontemps et al. (2010), but also towards Galactic infrared-quiet clumps, such as G28.34+0.06 P1 (Zhang et al. 2015), and G11.11-0.12 P6 (Wang et al. 2014). Alternatively, the high core formation efficiency and a shallow core mass distribution could suggest an intrinsically top-heavy distribution of

high-mass protostars at the early phases. Considering the twelve highest mass cores with  $M_{\text{MDC}} = 150\text{--}400 M_{\odot}$  and an efficiency ( $\epsilon$ ) of 10 – 30% (e.g. Tanaka et al. 2016), we could expect a population of stars with a final stellar mass of  $M_{\star} \sim \epsilon \times M_{\text{MDC}} = 15\text{--}120 M_{\odot}$ , reaching the highest mass O-type stars.

## 6. Conclusions

We study the fragmentation of a representative selection of a homogenous sample of massive infrared-quiet clumps, and reveal a population of MDCs reaching up to  $\sim 400 M_{\odot}$ . A large fraction (77%) of clumps exhibit limited fragmentation, and host MDCs. The fragmentation of massive clumps suggests a large concentration of mass at small scales and a high CFE. We lack observational support for strong enough turbulence and magnetic field to keep the most massive cores virialized. Our results are consistent with entire cloud fragments in global collapse, while the origin of their pre-collapse mass reservoir still challenges current star formation models.

*Acknowledgements.* We thank the referee for constructive comments on the manuscript. This paper makes use of the ALMA data: ADS/JAO.ALMA 2013.1.00960.S. ALMA is a partnership of ESO (representing its member states), NSF (USA) and NINS (Japan), together with NRC (Canada), NSC and ASIAA (Taiwan), and KASI (Republic of Korea), in cooperation with the Republic of Chile. The Joint ALMA Observatory is operated by ESO, AUI/NRAO and NAOJ. T.Cs. acknowledges support from the *Deutsche Forschungsgemeinschaft*, DFG via the SPP (priority programme) 1573 'Physics of the ISM'. HB acknowledges support from the European Research Council under the Horizon 2020 framework program via the ERC Consolidator Grant CSF-648505. LB acknowledges support from CONICYT PFB-06 project. A.P. acknowledges financial support from UNAM-DGAPA-PAPIIT IA102815 grant, México.

## References

- André, P., Di Francesco, J., Ward-Thompson, D., et al. 2014, *Protostars and Planets VI*, 27
- André, P., Men'shchikov, A., Bontemps, S., et al. 2010, *A&A*, 518, L102
- Avison, A., Peretto, N., Fuller, G. A., et al. 2015, *A&A*, 577, A30
- Bastian, N., Covey, K. R., & Meyer, M. R. 2010, *ARA&A*, 48, 339
- Bertoldi, F. & McKee, C. F. 1992, *ApJ*, 395, 140
- Beuther, H., Henning, T., Linz, H., et al. 2015, *A&A*, 581, A119
- Bontemps, S., Motte, F., Csengeri, T., & Schneider, N. 2010, *A&A*, 524, A18
- Butler, M. J. & Tan, J. C. 2012, *ApJ*, 754, 5
- Chabrier, G. & Hennebelle, P. 2011, *A&A*, 534, A106
- Cortes, P. C., Girart, J. M., Hull, C. L. H., et al. 2016, *ApJ*, 825, L15
- Csengeri, T., Bontemps, S., Schneider, N., Motte, F., & Dib, S. 2011a, *A&A*, 527, A135
- Csengeri, T., Bontemps, S., Schneider, N., et al. 2011b, *ApJ*, 740, L5
- Csengeri, T., Bontemps, S., Wyrowski, F., et al. 2017, *ArXiv e-prints*
- Csengeri, T., Urquhart, J. S., Schuller, F., et al. 2014, *A&A*, 565, A75
- Falgarone, E., Troland, T. H., Crutcher, R. M., & Paubert, G. 2008, *A&A*, 487, 247
- Girart, J. M., Beltrán, M. T., Zhang, Q., Rao, R., & Estalella, R. 2009, *Science*, 324, 1408
- Goldreich, P. & Kwan, J. 1974, *ApJ*, 189, 441
- Kainulainen, J. & Tan, J. C. 2013, *A&A*, 549, A53
- Kramer, C., Stutzki, J., Rohrig, R., & Corneliussen, U. 1998, *A&A*, 329, 249
- Krumholz, M. R., Klein, R. I., & McKee, C. F. 2007, *ApJ*, 656, 959
- Longmore, S. N., Pillai, T., Keto, E., Zhang, Q., & Qiu, K. 2011, *ApJ*, 726, 97
- McKee, C. F. & Tan, J. C. 2003, *ApJ*, 585, 850
- Motte, F., André, P., & Neri, R. 1998, *A&A*, 336, 150
- Motte, F., Bontemps, S., Schilke, P., et al. 2007, *A&A*, 476, 1243
- Ossenkopf, V. & Henning, T. 1994, *A&A*, 291, 943
- Palau, A., Ballesteros-Paredes, J., Vázquez-Semadeni, E., et al. 2015, *MNRAS*, 453, 3785
- Palau, A., Fuente, A., Girart, J. M., et al. 2013, *ApJ*, 762, 120
- Peretto, N., Fuller, G. A., Duarte-Cabral, A., et al. 2013, *A&A*, 555, A112
- Pillai, T., Kauffmann, J., Wiesemeyer, H., & Menten, K. M. 2016, *A&A*, 591, A19
- Sánchez-Monge, Á., Cesaroni, R., Beltrán, M. T., et al. 2013, *A&A*, 552, L10
- Schneider, N., Csengeri, T., Bontemps, S., et al. 2010, *A&A*, 520, A49
- Schuller, F., Menten, K. M., Contreras, Y., et al. 2009, *A&A*, 504, 415
- Svoboda, B. E., Shirley, Y. L., Battersby, C., et al. 2016, *ApJ*, 822, 59
- Tackenberg, J., Beuther, H., Henning, T., et al. 2012, *A&A*, 540, A113
- Tan, J. C., Beltrán, M. T., Caselli, P., et al. 2014, *Protostars and Planets VI*, 149

- Tan, J. C., Kong, S., Butler, M. J., Caselli, P., & Fontani, F. 2013, *ApJ*, 779, 96  
 Tanaka, K. E. I., Tan, J. C., & Zhang, Y. 2016, *ArXiv e-prints*  
 Traficante, A., Fuller, G. A., Peretto, N., Pineda, J. E., & Molinari, S. 2015, *MNRAS*, 451, 3089  
 Wang, K., Zhang, Q., Testi, L., et al. 2014, *MNRAS*, 439, 3275  
 Wienen, M., Wyrowski, F., Menten, K. M., et al. 2015, *A&A*, 579, A91  
 Zhang, Q., Wang, K., Lu, X., & Jiménez-Serra, I. 2015, *ApJ*, 804, 141  
 Zhang, Q., Wang, Y., Pillai, T., & Rathborne, J. 2009, *ApJ*, 696, 268

- 
- <sup>1</sup> Max Planck Institute for Radioastronomy, Auf dem Hügel 69, 53121 Bonn, Germany e-mail: [csengeri@mpi-fr-bonn.mpg.de](mailto:csengeri@mpi-fr-bonn.mpg.de)  
<sup>2</sup> OASU/LAB-UMR5804, CNRS, Université Bordeaux, allée Geofroy Saint-Hilaire, 33615 Pessac, France  
<sup>3</sup> Institut de Planétologie et d'Astrophysique de Grenoble, Univ. Grenoble Alpes – CNRS-INSU, BP 53, 38041 Grenoble Cedex 9, France  
<sup>4</sup> Laboratoire AIM Paris Saclay, CEA-INSU/CNRS-Université Paris Diderot, IRFU/Sap CEA-Saclay, 91191 Gif-sur-Yvette, France  
<sup>5</sup> Max Planck Institute for Astronomy, Königstuhl 17, 69117 Heidelberg, Germany  
<sup>6</sup> Departamento de Astronomía, Universidad de Chile, Casilla 36-D, Santiago, Chile  
<sup>7</sup> Univ. Lyon, ENS de Lyon, Univ Lyon1, CNRS, Centre de Recherche Astrophysique de Lyon UMR5574, F-69007, Lyon, France  
<sup>8</sup> IRAM, 300 rue de la piscine, 38406, Saint-Martin-d'Hères, France  
<sup>9</sup> School of Physics and Astronomy, University of Exeter  
<sup>10</sup> Jodrell Bank Centre for Astrophysics, School of Physics and Astronomy, The University of Manchester, Manchester, M13 9PL, UK  
<sup>11</sup> Astrophysics Research Institute, Liverpool John Moores  
<sup>12</sup> Instituto de Radioastronomía y Astrofísica, Universidad Nacional Autónoma de México  
<sup>13</sup> School of Physics & Astronomy, Cardiff University  
<sup>14</sup> Departments of Astronomy and Physics, University of Florida  
<sup>15</sup> European Southern Observatory, Karl-Schwarzschild-Strasse 2, D-85748 Garching, Germany  
<sup>16</sup> INAF-Osservatorio Astrofisico di Arcetri, Largo E. Fermi 5, I-50125 Firenze, Italy University  
<sup>17</sup> IAPS-INAf, Via Fosso del Cavaliere, 100, 00133, Rome, Italy  
<sup>18</sup> School of Physical Sciences, University of Kent, Ingram Building, Canterbury, Kent CT2 7NH, UK

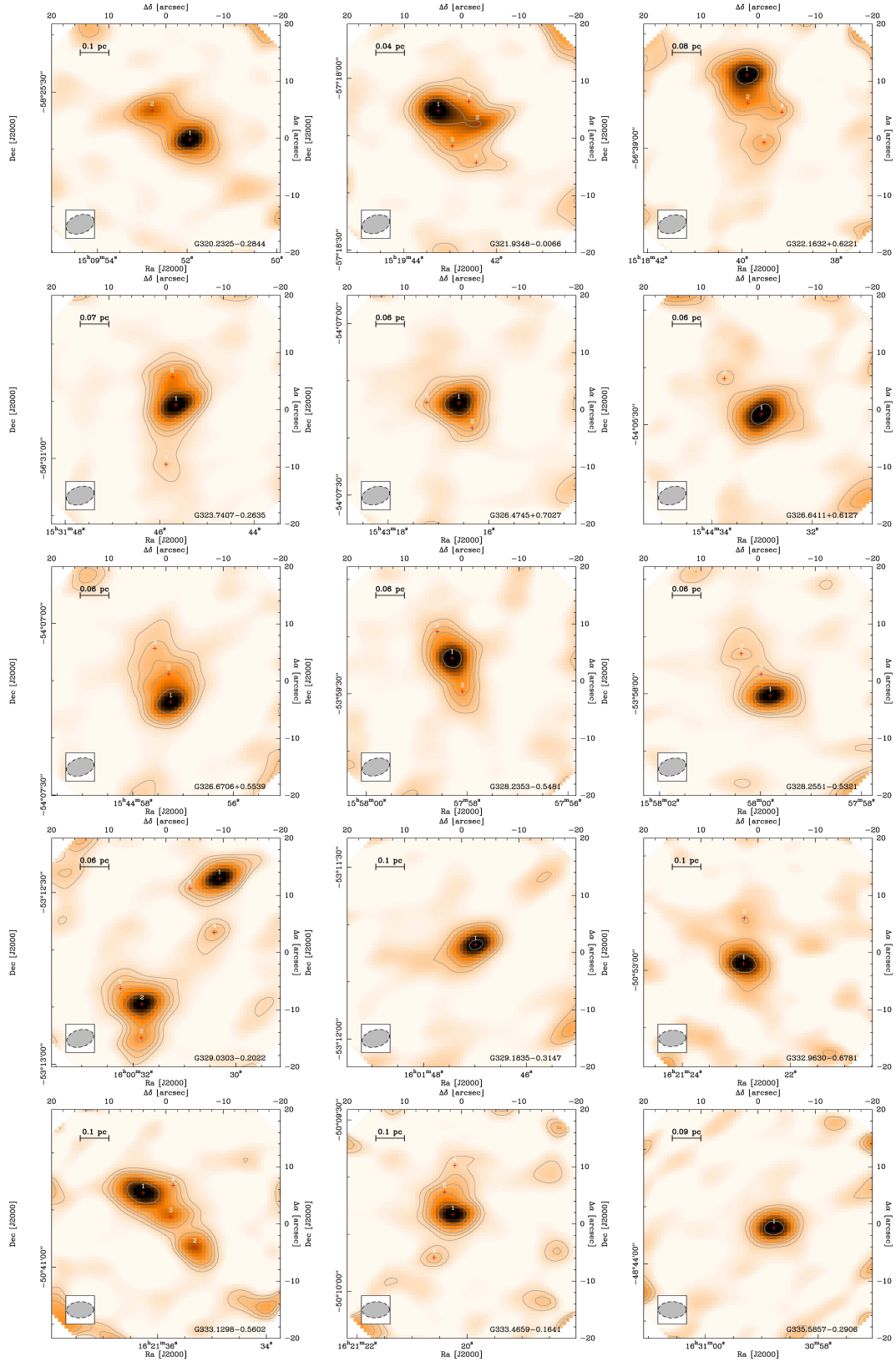


Fig. .1: Line-free continuum emission at 345 GHz with ALMA 7m array. Contours start at  $7\times$  the *rms* noise and increase in a logarithmic scale. Red crosses mark the continuum sources with labels in white (see Table 2). The beam is shown in the lower left corner of each panel.

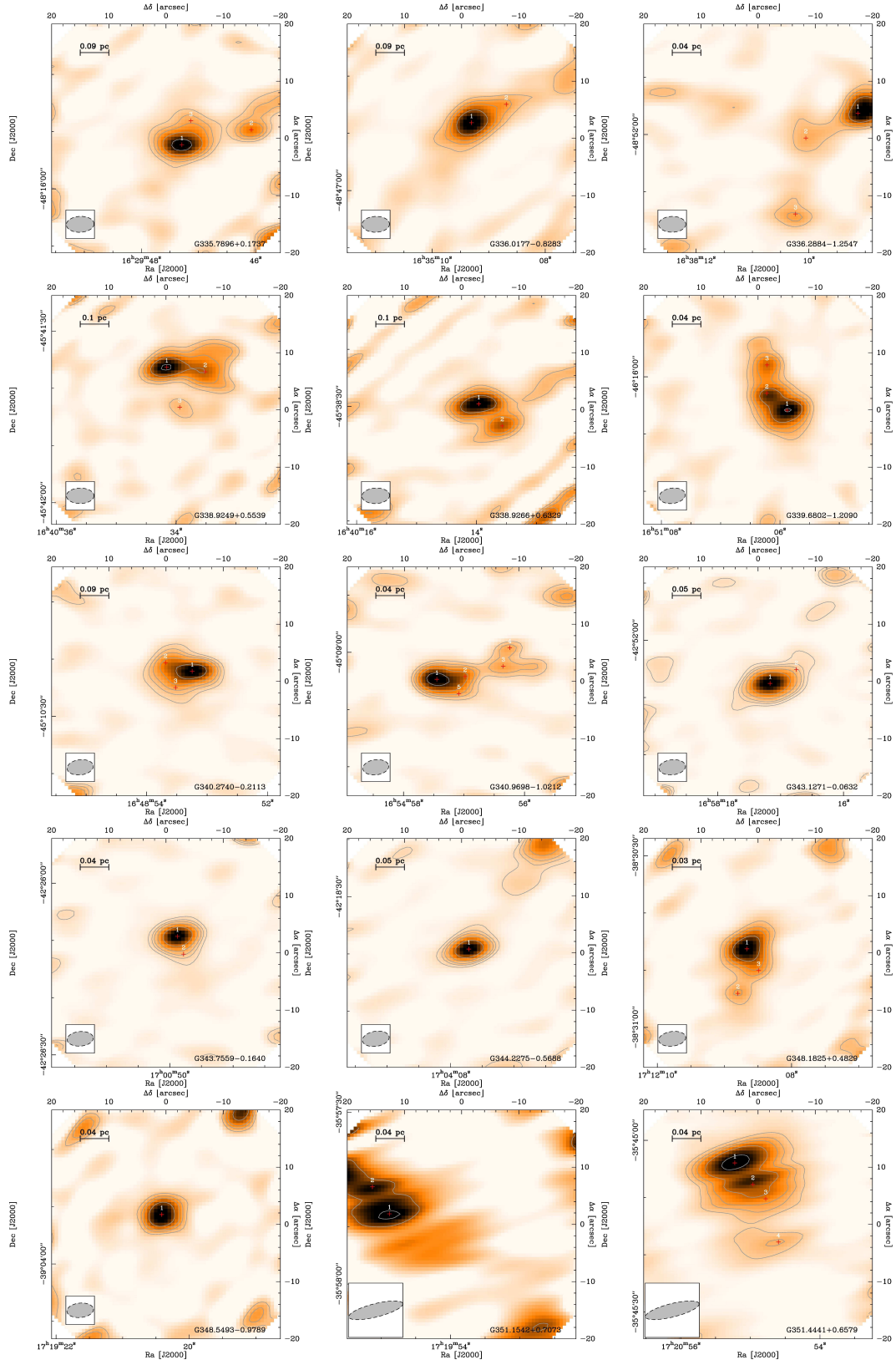


Fig. 1: Continued.

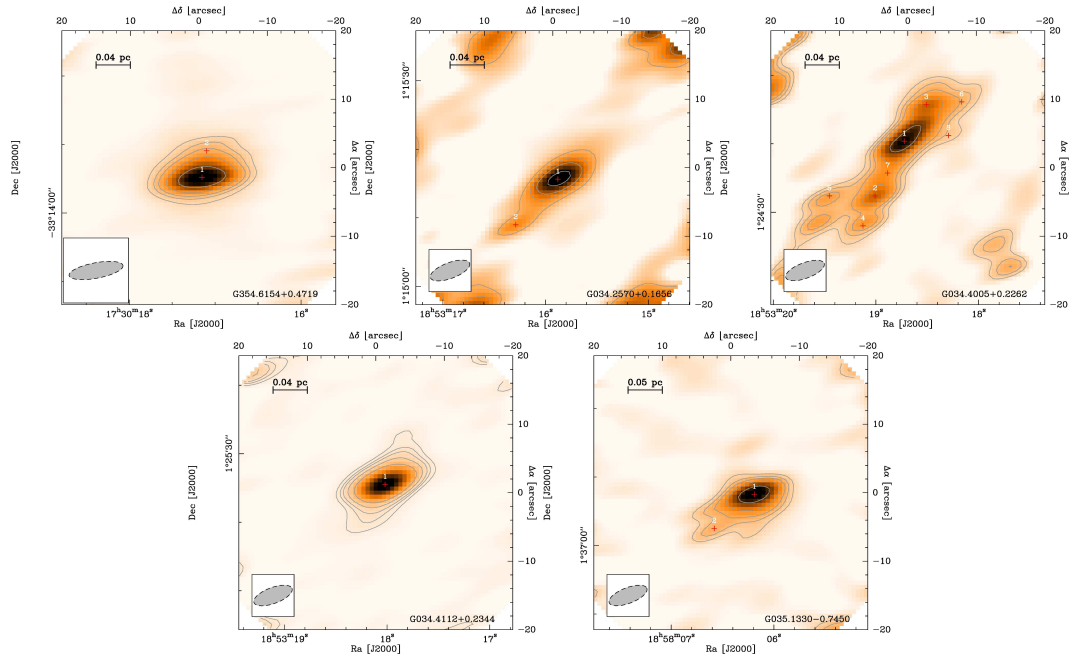


Fig. .1: Continued.



Table 2: Summary of physical properties of the sample.

Source	Position		$F_\nu$	$S_\nu$	$\Theta_A$	$\Theta_B$	beam	$FWHM$	$d$	$M_{\text{core}}$	$\Sigma_{\text{core}}$
	[RA J2000]	[DEC 2000]	[Jy/beam]	[Jy]	[ $''$ ]	[ $''$ ]	[ $''$ ]	[ $''$ ]	[kpc]	[ $M_\odot$ ]	[ $\text{g cm}^{-2}$ ]
320.2325-0.2844-MM1	227.46639	-58.42730	1.59	2.47	5.80	4.41	4.06	5.06	3.90	147.80	4.13
-MM2	227.46991	-58.42589	0.85	1.64	7.17	4.42	4.06	5.63	3.90	98.25	1.64
321.9348-0.0066-MM1	229.93021	-57.30158	1.24	2.65	6.47	5.18	3.97	5.79	1.80	33.68	2.27
-MM2	229.92670	-57.30223	0.75	1.48	7.17	4.35	3.97	5.58	1.80	18.84	1.46
-MM3	229.92896	-57.30329	0.32	0.61	6.98	4.33	3.97	5.50	1.80	7.74	0.64
-MM4	229.92747	-57.30112	0.28	0.37	3.79	5.60	3.97	4.61	1.80	4.76	1.04
-MM5	229.92681	-57.30411	0.21	0.31	7.17	3.18	3.97	4.77	1.80	3.93	0.67
322.1632+0.6221-MM1	229.66623	-56.64646	1.45	2.74	6.18	4.83	3.97	5.46	3.20	110.26	2.96
-MM2	229.66615	-56.64783	0.55	1.44	9.17	4.53	3.97	6.45	3.20	58.07	0.85
-MM3	229.66471	-56.64973	0.39	0.73	6.02	4.88	3.97	5.42	3.20	29.33	0.81
-MM4	229.66313	-56.64825	0.26	0.29	4.68	3.68	3.97	4.15	3.20	11.51	2.93
323.7407-0.2635-MM1	232.94024	-56.51407	2.77	5.10	6.52	4.38	3.94	5.34	2.80	157.05	5.95
-MM2	232.94057	-56.51270	1.12	1.81	7.09	3.53	3.94	5.00	2.80	55.78	2.90
-MM3	232.94111	-56.51695	0.38	1.21	6.19	7.97	3.94	7.02	2.80	37.13	0.54
326.4745+0.7027-MM1	235.81914	-54.12054	3.41	6.10	5.77	4.76	3.92	5.24	2.50	149.75	7.66
-MM2	235.81804	-54.12175	0.73	1.10	3.92	5.91	3.92	4.81	2.50	26.92	2.13
-MM3	235.82181	-54.12051	0.52	0.81	4.15	5.72	3.92	4.87	2.50	19.77	1.46
326.6411+0.6127-MM1	236.13754	-54.09115	1.85	4.42	5.09	7.10	3.89	6.01	2.50	108.45	3.20
-MM2	236.14062	-54.08943	0.31	0.55	5.41	4.99	3.89	5.20	2.50	13.62	0.71
326.6706+0.5539-MM1	236.23851	-54.12047	1.44	2.40	5.86	4.27	3.88	5.00	2.50	58.85	3.66
-MM2	236.23868	-54.11912	0.53	1.68	10.16	4.70	3.88	6.91	2.50	41.33	0.78
-MM3	236.23985	-54.11788	0.28	0.56	3.91	7.72	3.88	5.49	2.50	13.72	0.56
328.2353-0.5481-MM1	239.49290	-53.98994	1.99	3.83	5.43	5.18	3.82	5.30	2.50	94.10	4.31
-MM2	239.49205	-53.99156	0.63	1.36	5.28	5.98	3.82	5.62	2.50	33.30	1.22
-MM3	239.49412	-53.98866	0.38	0.60	3.52	6.49	3.82	4.78	2.50	14.69	1.10
328.2551-0.5321-MM1	239.49919	-53.96676	2.40	3.82	6.09	3.85	3.84	4.84	2.50	93.70	6.67
-MM2	239.50159	-53.96471	0.41	1.38	7.90	6.25	3.84	7.03	2.50	33.87	0.61
-MM3	239.49997	-53.96570	0.28	0.29	2.99	5.18	3.84	3.94	2.50	7.20	5.91
329.0303-0.2022-MM1	240.12633	-53.20764	1.80	2.70	5.90	3.68	3.80	4.66	2.50	66.38	5.65
-MM2	240.13261	-53.21375	1.76	2.89	5.70	4.15	3.80	4.86	2.50	70.86	4.76
-MM3	240.13267	-53.21539	0.63	1.28	6.18	4.75	3.80	5.42	2.50	31.45	1.31
-MM4	240.12675	-53.21026	0.39	0.55	3.90	5.20	3.80	4.50	2.50	13.49	1.43
-MM5	240.13436	-53.21298	0.38	0.78	3.83	7.76	3.80	5.45	2.50	19.14	0.78
-MM6 <sup>†</sup>	240.12874	-53.20814	0.24	0.22	3.50	3.83	3.80	3.80	2.50	5.44	0.23
329.1835-0.3147-MM1	240.44578	-53.19542	2.19	3.63	6.06	4.00	3.83	4.92	4.20	251.79	5.76
332.9630-0.6781-MM1	245.34527	-50.88301	1.37	2.50	5.75	4.30	3.68	4.97	4.20	172.85	3.41
-MM2	245.34521	-50.88081	0.29	0.79	5.46	6.69	3.68	6.04	4.20	54.60	0.52
333.1298-0.5602-MM1	245.40112	-50.67972	1.26	2.92	7.08	4.43	3.68	5.60	4.20	201.96	2.49
-MM2	245.39715	-50.68238	0.73	1.19	5.30	4.14	3.68	4.68	4.20	82.42	2.15
-MM3	245.39899	-50.68089	0.57	0.86	6.02	3.42	3.68	4.54	4.20	59.80	1.86
-MM4	245.39882	-50.67936	0.21	0.26	4.97	3.34	3.68	4.07	4.20	17.79	1.27
333.4659-0.1641-MM1	245.33441	-50.16293	2.26	3.69	5.64	3.89	3.67	4.68	4.20	255.59	6.62
-MM2	245.33505	-50.16183	0.64	1.23	8.01	3.23	3.67	5.09	4.20	84.98	1.50

Table 2: continued.

Source	Position		$F_\nu$	$S_\nu$	$\Theta_A$	$\Theta_B$	beam	$FWHM$	$d$	$M_{\text{core}}$	$\Sigma_{\text{core}}$
	[RA J2000]	[DEC 2000]	[Jy/beam]	[Jy]	[']	[']	[']	[']	[kpc]	[ $M_\odot$ ]	[ $\text{g cm}^{-2}$ ]
-MM3	245.33583	-50.16502	0.46	0.54	4.91	3.21	3.67	3.97	4.20	37.19	3.54
-MM4	245.33426	-50.16054	0.29	0.66	6.62	4.64	3.67	5.54	4.20	45.74	0.58
335.5857-0.2906-MM1	247.74493	-48.73158	4.53	7.11	5.64	3.91	3.75	4.70	3.80	403.36	13.52
335.7896+0.1737-MM1	247.44705	-48.26453	2.05	3.68	6.42	3.78	3.68	4.93	3.80	208.45	5.20
-MM2	247.44198	-48.26379	0.94	1.29	5.67	3.29	3.68	4.32	3.80	73.42	3.83
-MM3	247.44639	-48.26336	0.57	1.38	7.89	4.13	3.68	5.71	3.80	78.23	1.10
336.0177-0.8283-MM1	248.78877	-48.78004	2.73	6.23	6.38	4.76	3.65	5.51	3.80	353.15	5.56
-MM2	248.78620	-48.77915	0.84	1.38	5.80	3.78	3.65	4.68	3.80	78.32	2.44
336.2884-1.2547-MM1	249.53804	-48.86564	1.23	1.67	5.40	3.29	3.62	4.21	1.80	21.28	5.47
-MM2	249.54189	-48.86684	0.32	0.52	5.24	4.05	3.62	4.61	1.80	6.60	0.97
-MM3	249.54265	-48.87053	0.39	0.53	4.78	3.71	3.62	4.21	1.80	6.74	1.74
338.9249+0.5539-MM1	250.14232	-45.69342	2.53	4.11	6.22	3.40	3.61	4.60	3.90	245.59	7.70
-MM2	250.13965	-45.69364	1.38	3.31	5.93	5.27	3.61	5.59	3.90	197.56	2.76
-MM3	250.14142	-45.69537	0.59	0.98	6.00	3.60	3.61	4.65	3.90	58.46	1.74
338.9266+0.6329-MM1	250.05819	-45.64154	1.21	2.26	7.06	3.49	3.62	4.96	3.90	135.19	2.99
-MM2	250.05655	-45.64261	0.69	1.18	6.40	3.54	3.62	4.76	3.90	70.76	1.89
339.6802-1.2090-MM1	252.77450	-46.26829	1.05	2.04	5.80	4.12	3.51	4.89	1.80	25.97	2.68
-MM2	252.77592	-46.26746	0.69	1.05	5.27	3.54	3.51	4.32	1.80	13.39	2.53
-MM3	252.77591	-46.26609	0.55	0.92	5.02	4.12	3.51	4.55	1.80	11.77	1.68
340.2740-0.2113-MM1	252.22186	-45.17281	1.73	2.99	6.48	3.27	3.50	4.60	3.80	169.40	5.09
-MM2	252.22369	-45.17239	0.61	1.09	3.52	6.24	3.50	4.69	3.80	61.83	1.71
-MM3	252.22300	-45.17360	0.42	0.66	6.53	2.92	3.50	4.37	3.80	37.15	1.46
340.9698-1.0212-MM1	253.73937	-45.15131	2.22	3.93	5.69	3.76	3.48	4.63	1.80	49.95	6.42
-MM2	253.73742	-45.15118	0.93	1.31	4.62	3.69	3.48	4.13	1.80	16.64	4.02
-MM3	253.73480	-45.15067	0.68	1.25	6.05	3.70	3.48	4.73	1.80	15.91	1.85
-MM4	253.73435	-45.14978	0.56	0.58	4.65	2.69	3.48	3.54	1.80	7.33	20.95
-MM5	253.73785	-45.15201	0.38	0.61	6.18	3.16	3.48	4.42	1.80	7.78	1.25
343.1271-0.0632-MM1	254.57153	-42.86876	5.03	8.41	6.01	3.43	3.51	4.54	2.00	132.15	15.45
-MM2	254.56979	-42.86809	0.58	1.28	4.76	5.71	3.51	5.21	2.00	20.07	1.31
343.7559-0.1640-MM1	255.20783	-42.43592	5.26	7.35	5.08	3.22	3.42	4.04	1.80	93.53	24.01
-MM2	255.20742	-42.43678	0.81	1.29	6.65	2.80	3.42	4.32	1.80	16.37	2.83
344.2275-0.5688-MM1	256.03213	-42.31088	7.54	9.88	5.29	3.07	3.52	4.03	2.00	155.15	39.12
348.1825+0.4829-MM1	258.03610	-38.51286	2.84	6.26	5.65	4.75	3.49	5.18	1.30	41.57	6.50
-MM2	258.03667	-38.51502	0.88	1.47	4.94	4.10	3.49	4.50	1.30	9.78	2.77
-MM3	258.03538	-38.51391	0.77	0.92	4.69	3.10	3.49	3.81	1.30	6.12	5.88
348.5493-0.9789-MM1	259.83506	-39.06427	1.50	3.29	5.43	4.74	3.43	5.07	1.80	41.80	3.59
351.4441+0.6579-MM1	260.23010	-35.75109	5.33	12.06	10.65	4.83	4.77	7.17	1.70	136.87	6.40
-MM2	260.22902	-35.75214	3.68	5.21	9.94	3.24	4.77	5.67	1.70	59.15	8.38
-MM3	260.22825	-35.75284	2.03	2.79	2.62	11.89	4.77	5.58	1.70	31.63	5.04
-MM4	260.22749	-35.75493	1.37	2.08	9.15	3.77	4.77	5.87	1.70	23.60	2.69
354.6154+0.4719-MM1	262.57147	-33.23189	3.63	6.16	8.46	3.63	4.26	5.54	1.70	69.86	7.45
-MM2	262.57124	-33.23081	0.97	2.60	11.53	4.23	4.26	6.98	1.70	29.50	1.29
351.1542+0.7073-MM1	259.97866	-35.96326	0.76	2.05	11.75	5.20	4.77	7.82	1.70	23.28	0.81

Table 2: continued.

Source	Position		$F_\nu$	$S_\nu$	$\Theta_A$	$\Theta_B$	beam	$FWHM$	$d$	$M_{\text{core}}$	$\Sigma_{\text{core}}$
	[RA J2000]	[DEC 2000]	[Jy/beam]	[Jy]	[']	[']	[']	[']	[kpc]	[ $M_\odot$ ]	[ $\text{g cm}^{-2}$ ]
-MM2	259.97969	-35.96195	0.63	0.64	6.25	3.68	4.77	4.80	1.70	7.23	37.93
034.2570+0.1656-MM1	283.31617	1.25434	1.23	2.16	6.94	3.56	3.75	4.97	1.56	20.62	3.09
-MM2	283.31788	1.25249	0.50	0.68	2.67	7.18	3.75	4.38	1.56	6.46	2.01
034.4112+0.2344-MM1	283.32508	1.42376	4.41	5.97	6.30	2.98	3.72	4.33	1.56	57.06	18.50
035.1330-0.7450-MM1	284.52579	1.61874	1.18	1.93	6.81	3.22	3.67	4.68	2.19	36.29	3.47
-MM2	284.52742	1.61736	0.30	0.46	2.86	7.13	3.67	4.52	2.19	8.69	1.01
034.4005+0.2262-MM1	283.32802	1.41122	0.80	1.71	8.25	3.53	3.69	5.40	1.56	16.36	1.68
-MM2	283.32920	1.40900	0.49	0.81	6.76	3.37	3.69	4.77	1.56	7.75	1.35
-MM3	283.32712	1.41270	0.42	0.64	6.24	3.33	3.69	4.56	1.56	6.16	1.38
-MM4 <sup>†</sup>	283.32969	1.40778	0.29	0.29	2.31	5.87	3.69	3.69	1.56	2.74	0.32
-MM5	283.33105	1.40900	0.25	0.27	2.29	6.49	3.69	3.86	1.56	2.62	3.43
-MM6	283.32569	1.41281	0.18	0.31	3.67	6.40	3.69	4.85	1.56	2.95	0.48
-MM7 <sup>†</sup>	283.32869	1.40993	0.13	0.08	2.28	3.77	3.69	3.69	1.56	0.79	0.09
-MM8	283.32622	1.41144	0.14	0.19	6.35	3.00	3.69	4.36	1.56	1.81	0.53

**Notes.** <sup>(†)</sup> Unresolved sources.

The full table is available in electronic form at the CDS via anonymous ftp to cdsarc.u-strasbg.fr (130.79.125.5) or via <http://cdsweb.u-strasbg.fr/cgi-bin/qcat?J/A&A/>. Column 1 gives the source name, column 2 and 3 lists the position in J2000 equatorial coordinates. Column 4 and 5 give the peak and integrated flux densities, columns 6 and 7 give the FWHM major and minor axes. Column 8 gives the beam size as the geometric mean of the beam major and minor axes. Column 9 gives the beam convolved angular source size. Column 10 gives the distance from Csengeri et al. (2017). Column 11 and 12 give the core mass and surface density as described in the main text.